On the accuracy of automated shoreline detection derived from satellite imagery
A case study of the Sand Motor mega-scale nourishment

Hagenaars, Gerben; de Vries, Sierd; Luijendijk, Arjen; de Boer, Wiebe; Reniers, Ad

DOI
10.1016/j.coastaleng.2017.12.011

Publication date
2018

Document Version
Accepted author manuscript

Published in
Coastal Engineering

On the accuracy of automated shoreline detection derived from satellite imagery: A case study of the Sand Motor mega-scale nourishment

Gerben Hagenaars[a,1], Sierd de Vries[b], Arjen P. Luijendijk[a,b], Wiebe P. de Boer[a,b], Ad J.H.M. Reniers[b]

[a]*Deltares, Boussinesqweg 1, 2629 HV Delft*
[b]*Delft University of Technology, Stevinweg 1, 2628 CN Delft*

Abstract

Measured trends and variability in shoreline position are used by coastal managers, scientists and engineers to understand and monitor coastal systems. This paper presents a new and generic method for automated shoreline detection from the largely unexplored collection of publicly available satellite imagery. The position of the obtained Satellite Derived Shoreline (SDS) is tested for accuracy for 143 images against high resolution in-situ data along a coastal stretch near the Sand Motor, a well-documented mega-scale nourishment along the Dutch coast. In this assessment, we quantify the effects of potential inaccuracy drivers such as the presence of clouds and wave-induced foam. The overall aim of this study is to verify whether the SDS is suitable to study structural coastline trends for coastal engineering practice.

In the ideal case of a cloud free satellite image without the presence of waves, with limited morphological changes between the time of image acquisition and the date of the in-situ measurement, the accuracy of the SDS is with subpixel precision (smaller than 10 - 30 m, depending on the satellite mission) and depends on intertidal beach slope and image pixel resolution. For the highest resolution images we find an average offset of 1 m between the SDS position and the in-situ shoreline in the considered domain. The accuracy deteriorates

[1]Corresponding author.

in the presence of clouds and/or waves on the image, satellite sensor corrections and georeferencing errors. The case study showed that especially the presence of clouds can lead to a considerable seaward offset of the SDS of multiple pixels (e.g. order 200 m). Wave-induced foam results in seaward offsets in the order of 40 m.

These effects can largely be overcome by creating composite images, which results in a continuous dataset with subpixel precision (10 - 30 m, depending on the satellite mission). This implies that structural trends can be detected for coastlines that have changed with at least the pixel resolution within the considered timespan.

Given the accuracy of composite images along the Sand Motor in combination with the worldwide availability of public satellite imagery covering the last decades, this technique can potentially be applied at other locations with large (structural) coastline trends.

Keywords: Automated shoreline detection, Satellite imagery, Google Earth Engine, NASA, ESA, Positional accuracy, Coastline trends, Coastal management, Dutch coast, Sand Motor

2017 MSC: 00-01, 99-00

1. Introduction

The position and evolution of the shoreline along a coastal stretch is important to coastal managers, communities, scientists and engineers. Information obtained from trends and variability in the shoreline position, reveals information on beach variations and is used in coastal zone monitoring, policy making and the design of human interventions. Traditionally, the location of the shoreline is derived from aerial photography or video imagery (such as for instance used in Pianca et al. (2015)) or from in-situ measurements of the beach topography, such as used by Ruggiero et al. (2005), de Schipper et al. (2016) and Turner et al. (2016). According to the two main categories of shoreline definitions by Boak & Turner (2005), the shoreline from aerial photography or video imagery is based on a line that is visible to the human eye and the shoreline from in-situ measurements is based on a common datum or beach volume.

Whereas the collection of traditional shoreline datasets is often expensive and constrained in time and/or space, publicly available satellite imagery provides information on shorelines worldwide for the past 33 years. Potentially this data source is a valuable addition to traditional shoreline datasets, especially at locations where limited measurements are available. Until recently, obtaining shorelines from satellite imagery used to be laborious, which limited the use of this dataset to its full spatial and temporal extent. Moreover, a comprehensive study on the accuracy of satellite derived shorelines in relation to obtaining structural coastline trends is not yet available, which hampers the use in practice.

Recently Google launched the Earth Engine platform (GEE) that overcomes the traditional limitations in the usage of satellite imagery. Having both a petabyte satellite image collection and parallel computation facilities combined on the server side of the platform reduces image processing time to only several minutes per image (Gorelick et al., 2017). This increase in processing performance makes it possible to use the full collection of satellite images and allows for the opportunity to perform state-of-the-art image processing techniques such as image compositing (Hansen et al., 2013).

Image processing techniques are available to automatically derive a so called Satellite Derived Shoreline (SDS) position from satellite imagery (García-Rubio et al., 2015). The quality of this position may be prone to disturbances such as cloud cover, foam caused by surf and atmospheric interactions. The positional accuracy of a SDS position may therefore deteriorate by these disturbances, which may hamper retrieving coastline trends. Understanding and quantifying the positional accuracy of SDS positions is essential, and is assessed in for instance Bayram et al. (2008), Kuleli et al. (2011), Pardo-Pascual et al. (2012), García-Rubio et al. (2015), Almonacid-Caballer et al. (2016) and Liu et al. (2017). However, these studies are often limited by the amount of images used, the quality of the in-situ data or the limited range of changes in coastline locations along the coastal stretch. A comprehensive study on the accuracy of SDS positions and coastline trends using a large amount of satellite images is lacking.

To investigate the application range of SDS, we quantify the positional accuracy of an automatically derived SDS for an unprecedented 143 publicly available satellite images. Furthermore, we quantify the offsets in the SDS caused by clouds and waves. We do this by comparing the SDS position to in-situ data for the Sand Motor mega-nourishment. This case study is selected because of its dynamic behavior, which shows significant coastline changes over time and the availability of unique high resolution in-situ measurements to be able to validate the obtained shoreline position and trend.

2. Study site and data availability

The study site is the coastal stretch directly near the Sand Motor nourishment, comprising about 4.5 km of coastline length (Figure 1). This coastal stretch has an erosive character, which resulted in an extensive nourishment program to maintain a stable coastline. In 2011, a pilot mega-scale nourishment called the Sand Motor was put into place in front of the city of Kijkduin, which provides the adjacent coast with sediments for the coming 20 years (Stive et al., 2013).

An average tidal range of 1.7 m and a mean significant wave height of 1.3 m (Wijnberg, 2002) are observed along the Sand Motor. After 18 months, a landward shift of 150 m was observed near the tip of the sand motor, accompanied with an alongshore spreading of about 4 km (de Schipper et al., 2016). Focusing of wave energy is observed near the tip of the peninsula, leading to a local steepening of the beach profile. After the first storm season, a tidal lagoon developed with a tidal channel extending in the northern direction that shifts course over time.

High resolution and frequently measured in-situ data on the dynamic development of the topography and hydrodynamics is amply available for the Sand

Motor. Validating the position along such a dynamic study site against high resolution in-situ data provides new insight into the applicability of the SDS detection method to study equally or less dynamic coastal areas. The Sand Motor case is studied for the period 2011-08-01 (just after completion of the nourishment) to 2016-07-01.

Figure 1: Overview of the Dutch Delfland coastal cell bordered by Hoek van Holland (left) and Scheveningen (right). The Sand Motor study site is indicated in red. Depths at the -8 m, -5 m and +2 m NAP iso-contours are indicated in grey. The underlying satellite image (SPOT mission) was acquired on 18-05-2014. The water level measurement stations of Hoek van Holland and Scheveningen are indicated by means of a red dot. A nearshore point at the -10 m NAP depth contour, on which nearshore wave data are available, is indicated in yellow.

The SDS position is compared to concurrent in-situ measurements of the shoreline, obtained from topographic surveys and water level measurements. The topographic survey of the Sand Motor has been conducted on a monthly basis for the first year after completion and on a bi-monthly basis until present, resulting in a total of 36 topographic surveys. The topography of the Sand Motor study site is measured along transects spaced alongshore by 30 - 60 m (de Schipper et al., 2016). All available Landsat 5 (Thematic Mapper, TM), Landsat 8 (Operational Land Imager, OLI), Landsat 7 (Enhanced Thematic Mapper, ETM+) and Sentinel 2 images for the Sand Motor study site are listed in Table 1. The Landsat 7 Scan Line Corrector (SLC) failed in May 2003, resulting in large data distortions of the image (Wijedasa et al., 2012). Since the analysis period is after the SLC failure, the Landsat 7 images are left out of the analysis.

Water level measurements that include both tide and surges are obtained

Satellite mission	Sensor	Number of images	Pixel resolution [m]	Temporal extent
Sentinel 2 (A)		40	10 x 10	> 2015-07
Landsat 8	OLI	99	30 x 30	> 2013-04
Landsat 7	ETM+	112	30 x 30	> 2011-08
Landsat 5	TM	4	30 x 30	1984-01 - 2011-10

Table 1: Overview of the amount of satellite images per satellite mission available for the Sand Motor study area in the period of 2011-08-01 to 2016-07-01.

from the measurement stations at Hoek van Holland and the port of Scheveningen. These stations are located adjacent to the coast by about 10 km south and 7 km north with respect to the tip of the peninsula. Offshore wave data (wave height, period and direction) are obtained from the IJmuiden (located 56 km offshore) and Europlatform (located 62 km offshore) measurement stations. A nearshore significant wave height is found using a Simulating WAves Nearshore (SWAN) model (Booij et al., 1999), which transforms wave characteristics from the offshore measurement stations to the tip of the Sand Motor peninsula at the - 10 m NAP depth contour (Figure 1). Offshore wave records that are directed between 30 and 200 degrees North (indicating offshore directed waves) are not considered by the model and result in an absence of nearshore wave characteristics at the - 10 m NAP depth contour.

3. Methodology

The methodology to study the SDS positional accuracy and application in coastline monitoring practice can be subdivided into five steps: 1) automatic and unsupervised detection of the SDS position and calculation of its position relative to in-situ data; 2) definition of a benchmark case, in which all drivers that can cause inaccuracies are absent; 3) quantification of the drivers of inaccuracy in relation to the positional accuracy, 4) effect of an image composite processing technique on the mitigation of these drivers and 5) comparison between the long term coastline trend based on the SDS and in-situ shoreline data.

3.1. *Calculating the SDS positional accuracy*

Image processing

The individual satellite images are processed into SDS vectors in an unsupervised, automated way on the GEE servers. The approach used by Kuleli et al. (2011) is adopted and adjusted for this routine (Figure 2).

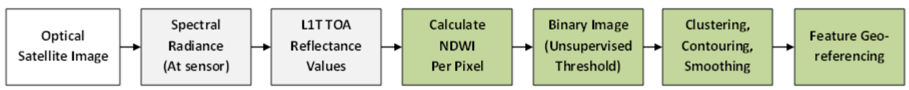

Figure 2: Satellite image processing steps in order to obtain a SDS position from an optical satellite image. The steps indicated in grey are end-user products provided by GEE. The steps indicated in green are performed per satellite image by the routine used in this study.

Firstly, the pixel values recorded by the satellite sensors for a particular optical satellite image are transformed to spectral radiance values using calibration coefficients made available by the satellite operator in the metadata. Secondly, the pixel radiance values are transformed to Top-Of-Atmosphere (TOA) reflectance values. The satellite image is orthorectified, resulting in a L1T TOA satellite image. These steps are preprocessed and made available as image products by the GEE.

Per pixel the Normalized Difference Water Index (NDWI) (Mcfeeters, 1996) value is calculated according to:

$$NDWI = \frac{\lambda_{NIR} - \lambda_{Green}}{\lambda_{NIR} + \lambda_{Green}} \tag{1}$$

in which λ_{NIR} $[nm]$ indicates the TOA reflectance value in the Near Infra-Red (NIR) band (band B4 in case of Landsat 5, band B5 in case of Landsat 8 and band B8 in case of Sentinel 2) and λ_{Green} $[nm]$ indicates the TOA reflectance value of the green band (bands B2, B3 and B3).

Calculating the NDWI value per pixel results in a greyscale image with NDWI values ranging from -1 to 1. This greyscale image is classified into a binary water-land image using the unsupervised greyscale classification method proposed in Otsu (1979). This method finds the optimal threshold value based on the statistical properties of the NDWI histogram. An example of such a NDWI histogram and the optimal threshold for a particular satellite image is displayed in Figure 3. In this example, a threshold value of -0.16 is found to separate the NDWI values into two distinct regions in the most optimal manner. All NDWI values smaller than this threshold value are classified as water and all NDWI values larger than this value are classified as land.

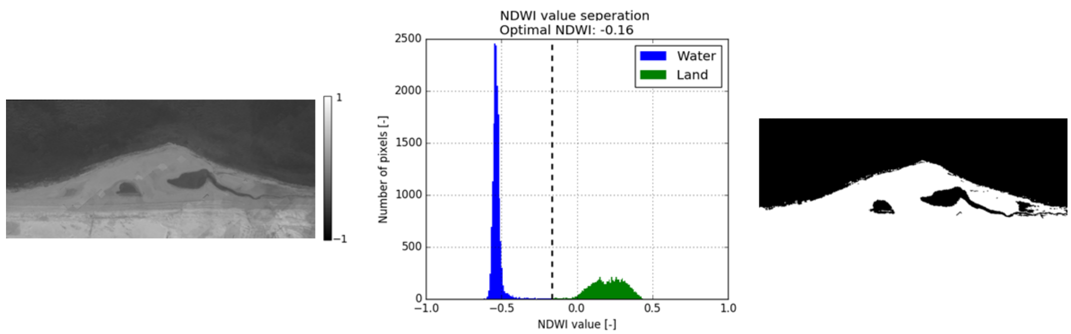

Figure 3: NDWI greyscale image (left), NDWI histogram (middle) and resulting binary image (right) for a Sentinel 2 image acquired on 12-03-2015 10:33:27 (GMT). An optimal threshold value of -0.16 classifies the NDWI values into water (blue) and land (green) pixels.

To cluster all pixels identified as water into a coherent water mask, a region growing algorithm is applied (Kamdi & Krishna, 2011). This algorithm starts at a random pixel identified as water and searches for neighboring pixels with the same classification. The outer edge of the obtained water mask is defined as the location of the SDS. This vector follows a saw tooth pattern since it is defined at the image pixel edges. The SDS coordinates are smoothed using a 1D Gaussian smoothing operation to obtain a gradual shoreline. The region growing method results in several SDS vectors since also lakes and small channels are detected as the SDS. In this analysis, only the most seaward SDS position is analyzed per satellite image. An example of the resulting SDS for a Sentinel 2 image is displayed in Figure 4.

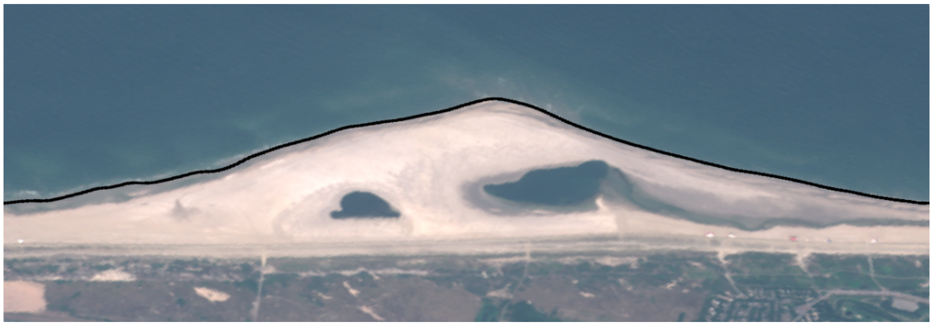

Figure 4: Satellite image acquired by the Sentinel 2 satellite acquired on 12-03-2015 10:33:27 (GMT) for the Sand Motor study site. The derived SDS is plotted in black.

The satellite images available on the GEE are georeferenced with respect to the first available image in the satellite mission. This allows for the study of changes, but since this first image is not necessarily positioned accurately with respect to the earth's surface, deviations are expected in case the position of the satellite image is compared to in-situ data. Manual georeferencing is therefore applied per satellite mission by means of six ground control points on a georeferenced aerial photo. Both horizontal translations and a rotation are applied based on the manual identification of these control points on a single cloud free satellite image per mission.

In-situ (survey) shoreline

The survey shoreline provides information on the actual waterline that was present during image acquisition and is reconstructed from in-situ topographic measurements. The reconstruction of the waterline is based on determining the intersection between the elevation of the Sand Motor's bed level with the water level elevation. The recorded Sand Motor elevations (as described in Section 2) are linearly interpolated on a rectangular grid with grid points spaced by 10 m (along shore) and 1 m (cross-shore) to obtain a continuous beach topography. The local water level near the Sand Motor is obtained using the water levels provided by the measurement stations of Hoek van Holland and Scheveningen. The water levels recorded during satellite image acquisition at both locations are linearly interpolated to the location of the Sand Motor. The iso-contour elevation that matches the water level is obtained using the Marching Squares Interpolation algorithm (MSI) (Mantz et al., 2008)). The survey shoreline is smoothed using a 1D Gaussian smoothing with the same properties as applied on the SDS. Figure 5 displays the interpolated topography and the resulting survey shoreline that matches the image acquisition date of the example Sentinel 2 image.

A nearshore significant wave height per image is found using the simulated nearshore wave climate at the tip of the Sand Motor peninsula at the - 10 m NAP depth contour (Figure 1), which is assumed representative for the wave climate in the study domain. This wave height in combination with a peak over threshold routine, is used to identify storm events. A storm wave height threshold value of 2.8 m, that coincides with a 99% exceedence probability, results in a total of 22 storm events in the studied period. Per satellite image a representative survey is found by means of nearest neighbor selection in time. In the case a storm event is identified based on the nearshore significant wave height in the period between the satellite image and the survey, the closest survey before the storm event is chosen. Because the survey measurement is conducted on a bi-monthly basis, the maximum number of days between a satellite image and the concurrent survey is 40 days.

Offset calculation

The buffer overlay method (Goodchild & Hunter, 1996) provides a robust routine to calculate the horizontal distance between two vectors. Since we assess both a continuous, curved SDS and survey shoreline, this method provides detailed and accurate information on the spatial offset. The method starts by defining a buffer with a certain width around the survey shoreline. The length of this buffer polygon intersected with the SDS is calculated. By increasing the buffer width, an increasing portion of the SDS position becomes enclosed by the buffer. The offset between the survey shoreline and the SDS is defined as the buffer that encloses 95% of the SDS (Figure 6). The method distinguishes

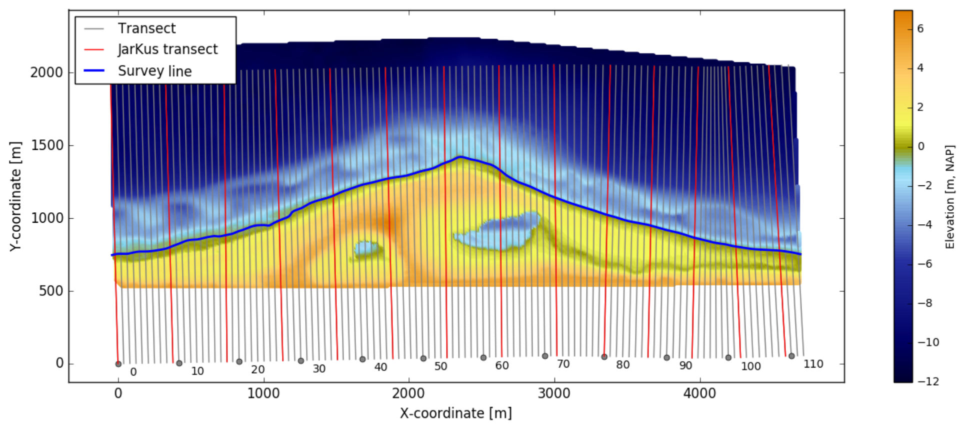

Figure 5: Interpolated topographic elevations and reconstructed survey shoreline for the 16-07-2015 Sentinel 2 satellite image. The measurement campaign to obtain the topography was conducted between 15-07-2016 and 17-07-2016. The transect system is indicated in grey and the JarKus transects are indicated in red. Every 10^{th} transect origin is indicated with a grey dot. Elevations are with respect to NAP, the national datum, which is about MSL.

between a landward and seaward offset, of which the largest value is stored.

System of transects

The study site is subdivided into smaller areas by means of a system of cross shore transects to obtain information on the spatial distribution of the offset. The buffer overlay offset calculation is performed for the area in between two transects. Along the Dutch coast, an official system of transects spaced alongshore by approximately 200 m is defined for the yearly coastal measurement campaign (JarKus, Jaarlijkse Kustlijnmeting) (Minneboo, 1995). Based on the orientation of these transects, a local system of transects is defined with an alongshore spacing of 40 m and a cross shore length of 2 km, resulting in a total of 113 transects for the study site (Figure 5). The alongshore spacing is in the range of the Landsat image pixel resolution and the acquisition of the survey topography.

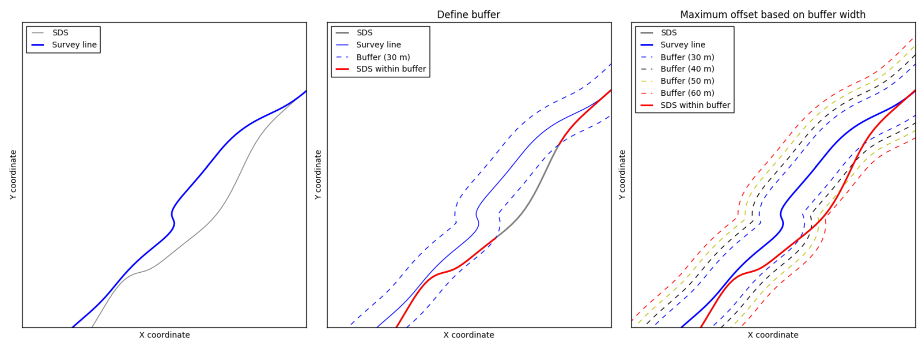

Figure 6: Buffer overlay offset routine to calculate the offset between the survey shoreline (blue) and the SDS (grey) using a buffer polygon (dashed line). The offset between the survey shoreline and the SDS is defined as the buffer that encloses 95% of the SDS.

3.2. Benchmark accuracy

The benchmark accuracy provides information on the best possible accuracy for the satellite sensors, the in-situ data and the applied offset calculation methodology. It is defined as the offset between the SDS of a cloud free image with calm wave conditions (e.g. a nearshore $H_{m0} < 0.5$ m) and a survey shoreline measured close to the time instance of the satellite image (e.g. within 10 days). This prevents surges and wave-induced foam from causing deviations in the linearly interpolated water level and morphological changes from deviations in the topography that was present during satellite image acquisition. The identified benchmark cases per satellite mission are listed in Table 2.

Table 2: Identified benchmark case characteristics per satellite mission. The Sentinel 2 imagery is provided by the European Space Agency (ESA). The Landsat imagery is provided by the National Aeronautics and Space Administration (NASA). Note that although the Landsat 5 benchmark has a 40% detected cloud cover near the shoreline, these are all thin, high altitude clouds that do not influence the shoreline position.

Mission	**Image**	**Survey**	**Cloud Cover**	**Wave height**	**Water level (surge**
Sentinel 2	2015-07-16 10:50:24	(15-17)-07-2015	0 %	0.47 m	-0.48 m (0.2 m)
Landsat 8	2015-03-19 10:39:36	(11-13)-03-2015	3 %	1 m	-0.53 m (0.16 m)
Landsat 5	2011-09-25 10:22:10	(03-05)-09-2011	40 %	0.18 m	0.12 m (0 m)

3.3. Drivers of inaccuracy

Often the benchmark accuracy cannot be obtained due to the presence of drivers of inaccuracy. 6 drivers are identified that cause the SDS position to deviate from the actual shoreline and hence increase the quantified offset. Drivers related to the environmental conditions on the image are: 1) cloud cover, 2) waves (surface roughness and foam) and 3) soil moisture and grain size (D_{50}). Drivers related to the satellite instrument are: 1) sensor corrections, 2) georeferencing and 3) image pixel resolution.

Optical satellite images are not able to acquire information of the earth under clouds, and hence contain no realistic information on the position of the SDS. Clouds have NDWI values in the range of land, resulting in a seaward offset of the SDS in case a cloud is present near the shoreline. Since foam caused by breaking waves has identical NDWI values as land, this also results in a seaward offset of the SDS beyond the breaker line in case foam is present close to the shoreline. Wet soils in combination with fine grains, as can be found in inter tidal zones along the Delfland coast, have NDWI values close to either land or water, making the unsupervised threshold based on the entire image less accurate. This can cause a landward offset in case wet intertidal zones are present (for instance during falling tide conditions).

Instrument related inaccuracies are caused by sensor corrections required to transform the observed sensor radiance to TOA reflectance values and to align the pixel locations. Errors caused in these procedures can be identified based on visual inspection. Georeferencing of the image is necessary since the projection of a 3D surface on a 2D image results in incorrectly aligned pixel locations. This is mitigated by means of orthorectification, in which the Global Land Survey Digital Elevation Model (GLS-DEM) (USGS, 2008) is used. However, since the used dataset on the EE server comprises a global dataset with a spatial resolution of 90 m and acquisition in 2005, local deviations are likely to be present. Georeferencing remains necessary when comparing satellite positions to in-situ data, and is performed in this study by means of ground control points. The image pixel resolution averages all reflectance values within a pixel to a single value. This means that the pixel resolution determines the level of detail present on the image, and hence contributes to the found offset value.

The effect of the drivers of inaccuracy on the offset values is quantified. Cloud cover is investigated by comparing the offsets of SDS positions obtained from images with a local cloud cover $\leq 5\%$ to images with a local cloud cover $> 5\%$. The effect of wave height is investigated by comparing SDS positions from cloud free images with calm wave conditions with a nearshore $H_{m0} \leq 0.5m$ to cloud free images with a nearshore $H_{m0} > 0.5m$. The effect of georeferencing is quantified using the satellite images processed by the GEE and shorelines obtained after applying the local georeferencing procedure. Sensor corrections are assessed by means of visual inspection. The effect of pixel resolution is quantified by comparison of Landsat (30 m pixel resolution) and Sentinel 2 images (10 m pixel resolution).

To detect clouds near the shoreline, the Fmask algorithm (Zhu et al., 2015) is used. This algorithm provides per pixel information on the presence of clouds for the Landsat 5, 7 and 8 images. A buffer polygon extending 400 m along a transect and 40 m alongshore is defined around the center of a transect. Within this buffer, the amount of pixels indicated as cloudy is used to obtain a cloud cover percentage per transect. Since information from the Fmask algorithm is absent in GEE in case of the Sentinel 2 images, pixels are set to cloudy values based on visual inspection and cloud cover values provided by the metadata. Information on the nearshore significant wave height obtained from the SWAN model output is used to identify calm and mild wave conditions. Because data on soil moisture and grain size are absent for the study site, these drivers are left out of the analysis.

3.4. Image composite technique

To reduce the satellite related drivers of inaccuracy such as cloud cover, waves, soil moisture and sensor corrections, Donchyts et al. (2016) used an image composite processing technique. This technique uses a sequence of satellite images to obtain a single composite image. Each pixel in the composite image is obtained from the 15^{th} percentile value of the TOA green and NIR reflectance values of the concurrent pixels within a sequence of individual images. This approach is based on the idea that clouds cause high reflection values and choosing the 15^{th} percentile value results in clear pixels (Figure 7).

The downside of the image composite technique is that multiple images over time are aggregated. Therefore, information on shoreline variability within the time sequence is lost to some extent. In order to find an optimal balance between the positional accuracy and the temporal variability, composite images using a moving average time sequence window of 90, 180, 360 and 720 days are used. To quantify the positional accuracy of the image composites, a composite survey shoreline is obtained by calculating an average topographic survey and water level from the time instances of the individual images within the time window.

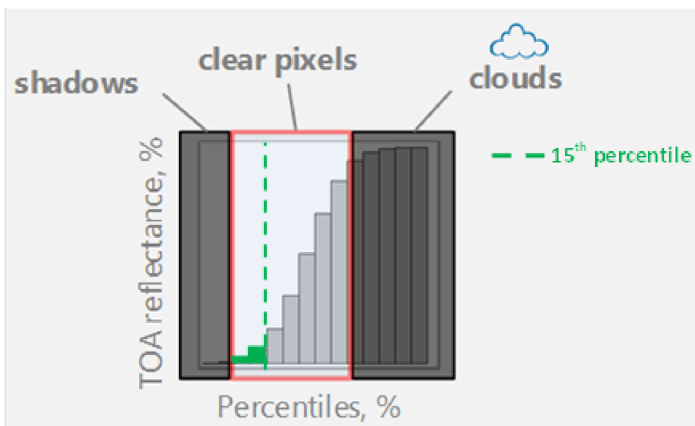

Figure 7: Principle of the image composite technique based on the distribution of all TOA reflectance values within the image composite time window per pixel. The 15^{th} percentile value is used throughout this study to obtain a composite image. Adjusted from: Donchyts et al. (2016)

3.5. Coastline trends

In order to monitor coastal evolutions characterized by a time series of SDS positions, the SDS vector is projected along the system of transects. This way the distance between the transect origin (as defined in Section 3.1) and the intersection point of the SDS with a transect is obtained. This distance is proposed to serve as a coastal indicator and changes in this distance over time reveal information on the dynamics at the shoreline. This is in line with the analysis used in the sectional calculation application on coastal monitoring (Thieler et al., 2009). To quantify trends, a fit through the data is made by means of Ordinary Least Squares (OLS) of the linear equation:

$$y(t) = at + b \tag{2}$$

in which $y(t)$ $[m]$ is the distance between the transect origin and the SDS intersection at time instance t, a $[m/y]$ is an indicator for the structural rate of change and b $[m]$ is the distance between the transect origin and the first SDS. a may be identified as an indicator for structural erosion or accretion and is quantitatively compared to the structural trend obtained in the same manner from the MSL (0 m NAP) contour retrieved from the topographic surveys.

4. Results

4.1. Benchmark accuracy

The calculated offset values for the benchmark case per satellite mission are displayed in Figure 8. An average offset of 1.3 m, 8.5 m and 1 m is found for the Sentinel 2, Landsat 8 and Landsat 5 benchmarks. This indicates subpixel precision and the absence of large offset values in case of Sentinel 2 and Landsat 5. The Landsat 8 benchmark has an average offset of about 1/3 of the pixel size, indicating a larger offset. The standard deviations of 5.1 m, 13.2 m and 13.9 m all indicate offset variations within a pixel and relate to half the image pixel resolution.

The inter tidal beach slope (Figure 8) ranges from 1:24 m to 1:200 m, indicating large alongshore variabilities. Similarities in the alongshore pattern of the inter tidal beach slope and the offset value can be observed, in which steep slopes are accompanied by small offset values and mild slopes are accompanied by larger offset values. This is clearly present in both the Sentinel 2 and Landsat

8 benchmark cases. This relation is less pronounced in case of Landsat 5, which might be due to the very rapid initial morphologic evolution in combination with the longer time difference between the topographic survey and satellite image acquisition (21 days).

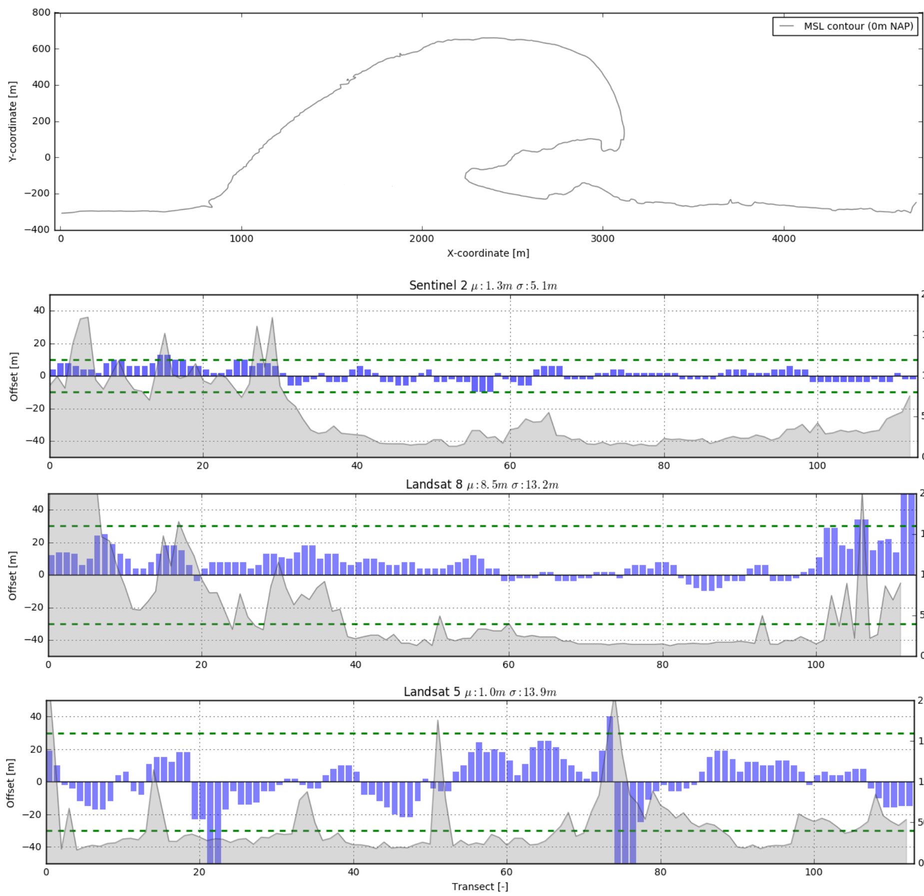

Figure 8: The top panel indicates the MSL elevation contour of the survey conducted on 03-08-2011. Offset result per transect for the Sentinel 2 (second panel), Landsat 8 (third panel) and Landsat 5 (bottom panel) benchmark cases. The image pixel resolution is indicated in green, the inter tidal beach slope per transect is plotted in grey.

The Landsat 5 benchmark case shows an average offset over all transects of 1 m with a standard deviation of 13.9 m. These values are obtained after removal of 5 evident outliers near transects 21 and 75 (Figure 9). The topography near transect 21 has a complex geometry, resulting in a survey shoreline that is not correctly extracted by means of the MSI method. Besides, this location of the Sand Motor had a different topography than present during satellite image acquisition, indicating that morphological changes contributing to the offset have occurred in the 21 days between conducting the survey and satellite image acquisition. This results in a large offset value of 64 m. The situation near transect 75 indicates that the survey shoreline does not include the tidal lagoon, whilst this is the case for the SDS. This is due to the survey shoreline extraction method, where only a single, most seaward intersection per transect is obtained.

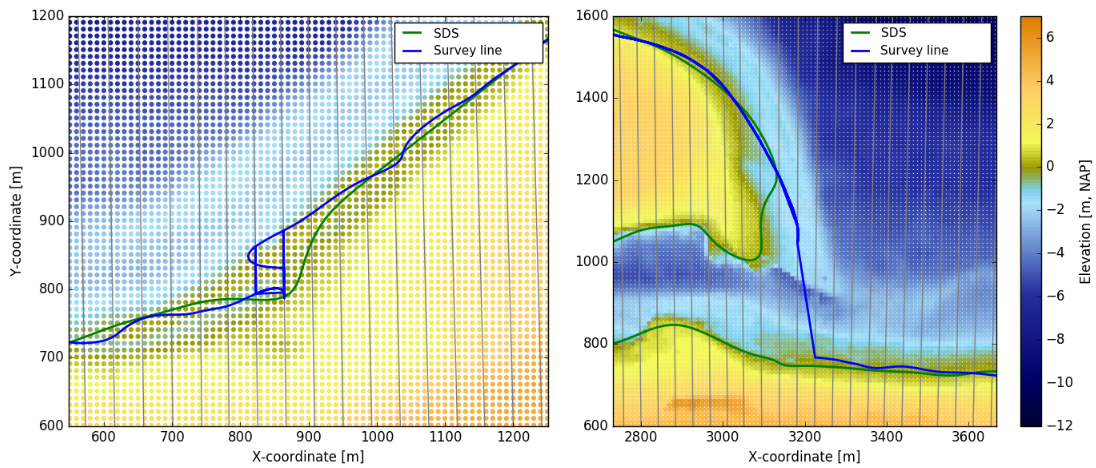

Figure 9: Zoom-in on the Landsat 5 benchmark case with the topography, the SDS (green) and the survey shoreline (blue). The left panel indicates the location near transect 21, the right panel indicates the location near transect 75. Please note that the scales of both panels are different.

4.2. Drivers of inaccuracy

All 143 satellite images are analyzed to quantify the drivers of inaccuracy related to the satellite environmental conditions. On the GEE platform, the analysis of all 143 images requires a total processing time of about 24 hours. Based on the 113 transects defined for the study area, this results in a total of

16,159 offset values (Figure 10). In this analysis, images with evident sensor errors (apart from Landsat 7 that is already omitted from the analysis) are neglected.

The first row indicates the offset values for all transects. When filtering the transects on local cloud cover (with a cloud free image defined based on a local cloud cover of $\leq 5\%$), the average offset (μ) reduces from 56.5 m to 21.9 m, which is below the pixel resolution of the Landsat missions. Besides, the standard deviation (σ) decreases, indicating a more constant offset. When the transects are filtered on both cloud cover and significant wave height (where calm wave conditions are defined based on a nearshore $H_{m0} \leq 0.5m$), the average and standard deviation reduce to 8.9 m and 17 m, respectively. The histogram remains positively skewed, indicating that more often the SDS is located seaward of the survey shoreline. This is in line with findings in for instance Pardo-Pascual et al. (2012). In case the transects are subdivided based on satellite mission, the same pattern in offset reduction occurs when filtered on environmental conditions (Figure 10). This indicates that the environmental sources of cloud cover and wave height cause the same effects on the offset values, despite the sensor. All missions combined reveal a positive skewed histogram, indicating a seaward bias of the SDS.

Cloud cover affects the detectability of the SDS position. 24 % of the transects that are marked as cloudy have a non-calculated offset value, meaning that an SDS position was absent. These values are not included in the offset distributions of Figure 10.

Sensor errors are identified manually. In case of seven Sentinel 2 images, a data gap covering about half the image domain was present. The locations of these gaps are identified as the location of the SDS by the region growing algorithm, and hence result in large offset values. In case of three Landsat 5 images, scattered sunlight reflections were present in all bands at some locations. Since these reflections are calculated as positive NDWI values, seaward offsets of the SDS are found.

The image pixel resolution hardly affects the average offset when comparing

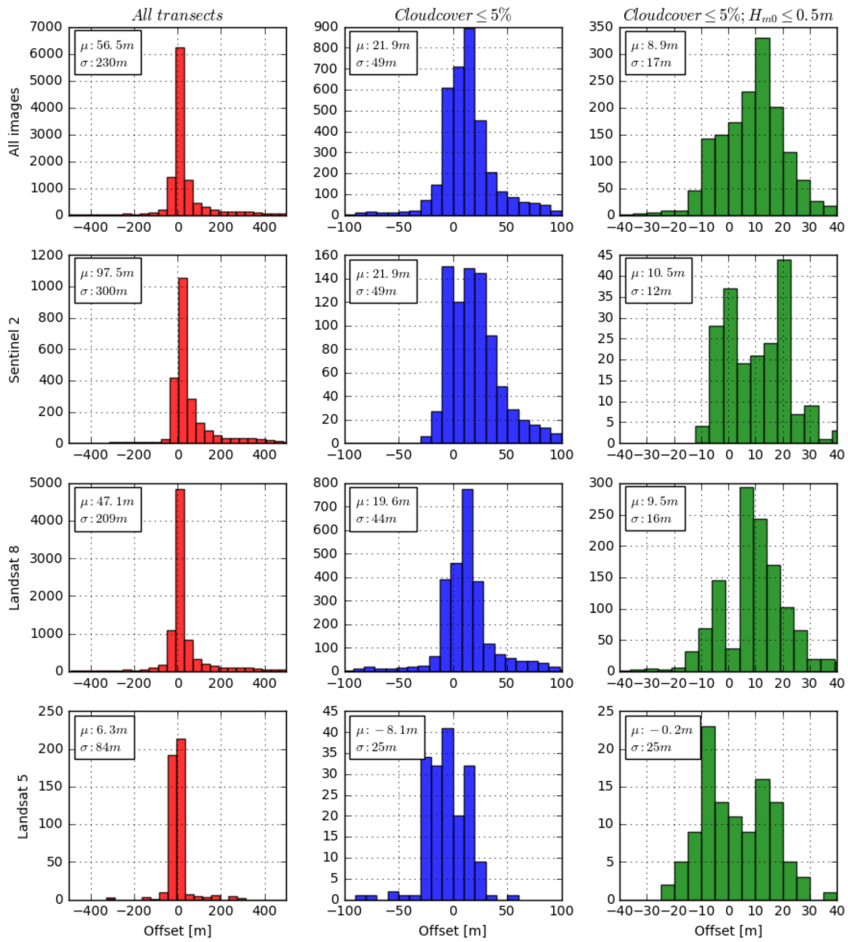

Figure 10: Overview of the offset calculation between all SDS positions and their concurrent survey shorelines. The first row contains the offset values for all satellite missions, the other rows contain the offset values per satellite mission. The second column indicates the result after filtering transects on local cloud cover, the third column indicates filtering on cloud cover and nearshore wave height. Please note the different x-axis limits per filter, which are the same for all missions.

Sentinel 2 to Landsat 8. In both cases an average offset of 9.5 and 10.5 m is found. The standard deviation reduces from 16 m in case of Landsat 8 to 12 m in case of Sentinel 2, indicating that the distribution of offset values relates to the image pixel resolution.

The effect of shifting the benchmark SDS positions as a result of the georeferencing procedure with respect to the standard georeferencing as applied on the GEE platform results in an offset reduction in case of Sentinel 2 and Landsat 5 (Figure 11). Because the translation shifts the SDS both alongshore and cross shore, the shape of the histogram also changes. In case of Landsat 8 the offset value increases after georeferencing. This indicates that the applied translation based on six control points is not sufficient to correctly align Landsat 8 and local deformations might be present.

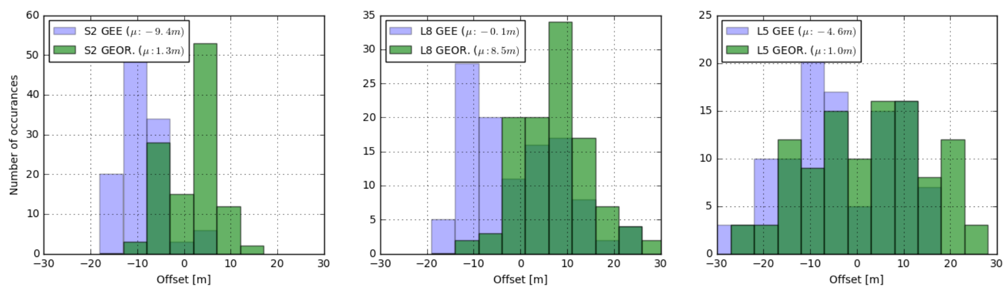

Figure 11: Overview of the offset calculation related to georeferencing before (GEE) and after georeferencing (GEOR.) for Sentinel 2 (first panel), Landsat 8 (second panel) and Landsat 5 (third panel).

4.3. Image composites

The effect of the moving average image composite technique with time windows of 90, 180, 360 and 720 days on the offset values is shown in Figure 12. Compared to the unfiltered individual images (top left panel of Figure 10) the average offset reduces from 56.5 m in case of individual images to 14.9 m in case of a 90 days image composite window. The tendency towards lower average offset values continues for larger windows. The offset standard deviation reduces from 36 m in case of a 90 days window to 18 m in case of a 720 days window. This indicates that the offset is on a subpixel level (e.g. 10 - 30 m, depending on the satellite mission) for all considered images in case of a longer averaging time window. This implies that the image composite technique has an accuracy in the order of one pixel, which makes the method suitable for the study of structural, yearly trends as long as these trends are larger than the pixel resolution. A drawback of aggregating multiple satellite images into yearly composites is that it reduces the detection of smaller scale variability, making longer windows less suitable for the detection of intra-annual trends. A seaward offset remains present in the offset values, indicating that the actual shoreline is positioned more landward than the SDS.

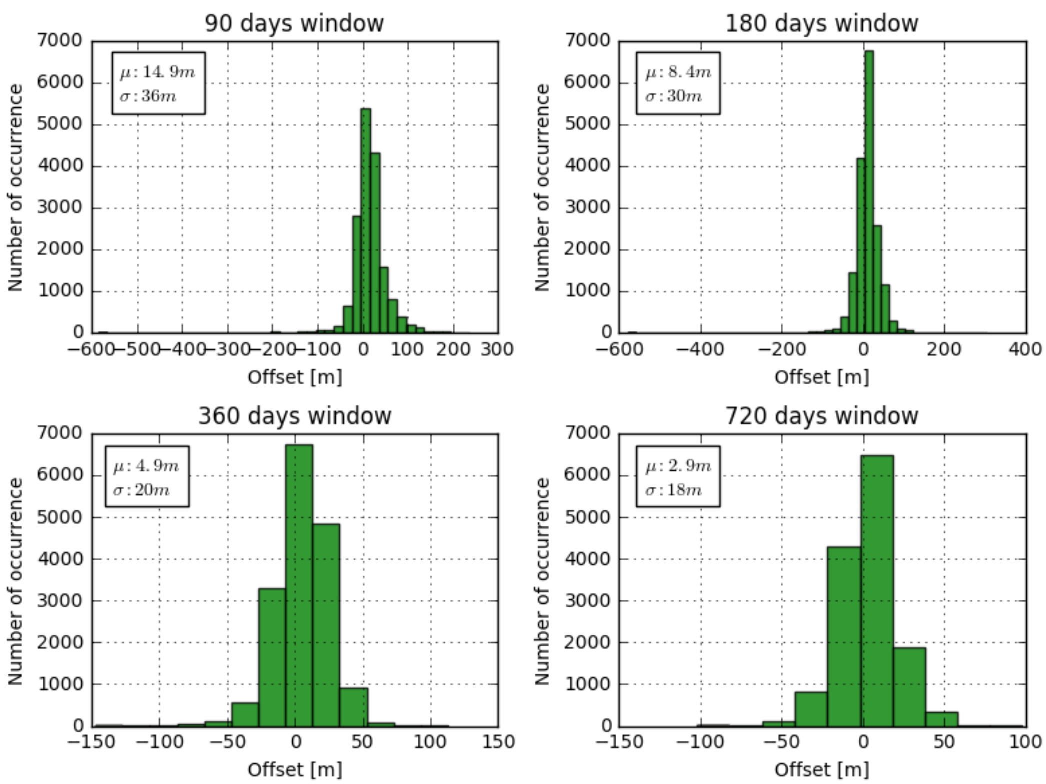

Figure 12: Overview of the offset values for all transects per image composite window of 90, 180, 360 and 720 days.

4.4. Coastline trends

In order to assess the suitability of the technique to identify structural trends in the shoreline position, the trends obtained from the SDS are compared to trends obtained from shorelines at MSL obtained from the topographic surveys. For this analysis the Landsat 8 and Sentinel 2 images are used. Landsat 5 is not considered since this would introduce a large gap of SDS positions in the period after the stop of Landsat 5 and the launch of Landsat 8, which hampers the OLS fit. The 360 days moving average time window provides offset values within a pixel and therefore still contains annual information. The subsequent SDS positions obtained from a 360 days moving average time window and MSL contour elevations obtained from the topographic surveys are projected along the system of transects. A monotonous eroding trend is visible for both data sources when using the thus obtained distance with respect to the transect origin for transect 54 (Figure 13). When OLS is applied for the period starting at 01-04-2013, which is after the start of Landsat 8, a landward (erosive) rate of change of 52.0 m/y is found in case of the survey MSL contour and 54.2 m/y in case of the SDS. This indicates that the same trends can be extracted from both data sources, and that a rate of change deviation of 2.2 m/y is found.

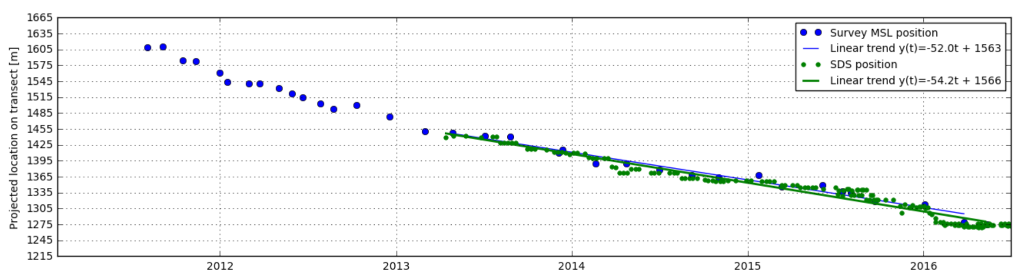

Figure 13: Timeseries of SDS positions the MSL contour lines obtained from the survey projected along transect 54. An OLS fit is made based on the information between 01-04-2013 and 01-07-2016.

Performing OLS and recording the rate of change value for all transects results in a spatial overview of erosion and accretion (Figure 14). All fits are based on the SDS period between 01-04-2013 and 01-07-2016. A landward trend is observed from transect 16 up to transect 80. Shoreline rates of change ranging between -57.0 m/y and 60.0 m/y are found along this study site. The maximum landward directed shoreline rate of change of -57.0 m/y is observed at the tip of the peninsula, indicating erosive behavior. Adjacent to the Sand Motor, seaward trends are visible, indicating that the adjacent coast is accreting.

In 110 of the 113 transects the direction of the trend is equal, indicating that landward and seaward trends are observed in both data sources even though the rate of change value shows deviations. Comparing the rate of change values obtained from the SDS and survey MSL contour shows an average difference of 6.1 m/y. This is predominantly caused by the positions located around transect 5 and at the tidal channel mouth near transect 90. Near transect 5 a strong periodic behavior is present, resulting in a less distinct rate of change based on OLS and hence a higher importance towards the exact timing of the survey topography in relation to the satellite imagery. When these transects are left out of the analysis, an average rate of change difference of 5.3 m/y is found. At first sight this difference may seem large, but, given the considered timespan of 5 years, this rate of change corresponds to a total deviation of 26.5 m. This deviation is within the pixel resolution, in line with findings in Section 4.3. A minimum deviation of 2.2 m/y is found at transect 54, where a monotonous shoreline change is present and the OLS fit performs well.

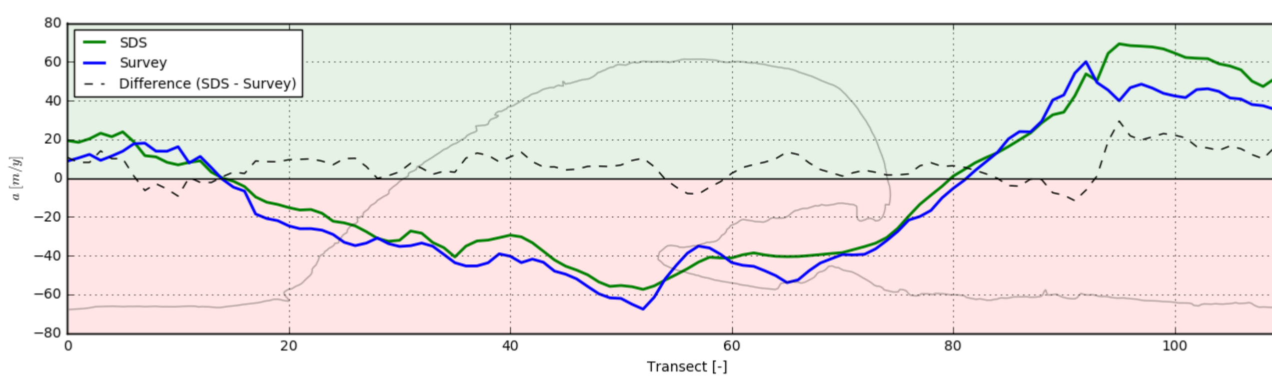

Figure 14: Alongshore rate of shoreline change (a) based on the SDS position (green) and the survey MSL contour (blue). The black line indicates the difference between a_{SDS} and a_{Survey}. The MSL contour line from the survey conducted on 03-08-2011 is plotted in grey as a reference.

5. Discussion

The survey shoreline is used in this study as the ground truth position to validate the positional accuracy of the SDS. Since the survey shoreline is reconstructed using measured elevations and the interpolated water level, inaccuracies in this representation of the shoreline contribute to the found offset value. These effects are reduced by using high resolution and frequent in-situ data. The water level is interpolated from the nearest measurement stations, which measure both the tidal elevation and local surge. However, local deviations in the water level are not accounted for and contribute to the found offset. These depressions can be due to for instance wave set-up and run-up or tidal dispersion (Radermacher et al., 2017), of which the large scale eddy may lead to local water level depressions. The survey that was conducted closest to the satellite image is used, taking into account the timing of storm events. The survey topography is interpolated to a rectangular grid that is finer than the satellite image pixel resolution. This ensures that the survey shoreline provides an accurate resemblance of the actual waterline. Since an alluvial, dynamic sandy beach is studied, morphological changes can be substantial, indicating the relevance of frequent survey campaigns in this accuracy assessment. To demonstrate the sensitivity of the offset on the local water level, we reconstruct the survey shoreline at the MSL (0 m NAP) contour rather than at the actual water level measured at the measurement stations. When this survey shoreline is compared to the SDS of the Sentinel 2 benchmark case, an average offset of 24 m with a standard deviation of 16 m is found, indicating offsets of multiple pixels.

The panchromatic band 8 of the Landsat 8 and Landsat 7 mission allows for the method of pansharping. This method uses both the high spectral resolution of the optical bands and the high spatial resolution of the panchromatic band to obtain multispectral information with a pixel resolution of 15 x 15 m. In this study the original Landsat 8 images are considered. To study the effect of pansharping on the offset of the Landsat 8 images, all SDS position from cloud free Landsat 8 satellite images are compared to their concurrent SDS positions obtained after pansharping. The average offset over all selected transects increases from 20 m to 41 m, which indicates that pansharping increases the offset to more than a pixel. This is counterintuitive since pansharping was introduced to increase the pixel resolution and hence to reduce the offset values.

Figure 15 shows the obtained shorelines for both the original and pansharped benchmark Landsat 8 image. As can be observed, pansharping adds additional NDWI information to the pixel values. A non-coherent portion of information is added near the shoreline, resulting in small portions of land detected as water and vice versa. This non coherent portion results in additional offsets when compared to the survey shoreline. This might have to do with the effect of pansharping on the NIR band and the absence of multispectral contrast near a sand-water transition.

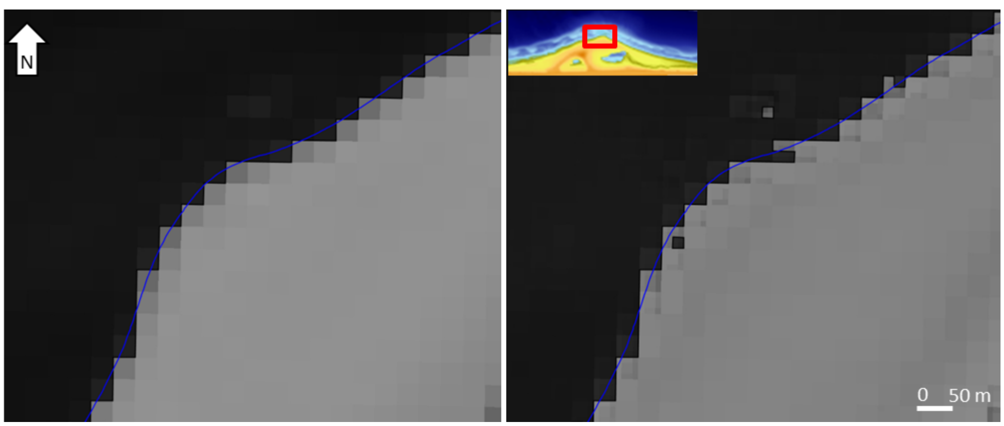

Figure 15: Effect of pansharping on the obtained SDS position. Top left shows the greyscale NDWI image and the obtained smoothed SDS position in blue on the Landsat 8 benchmark image. The right panel indicates the situation after pansharping.

The increasing moving average time window reduces the offset values (Figure 12). The survey shoreline that is used to compare the SDS position is based on the average water level and topography of all underlying satellite image time instances. However, some of these satellite images are cloudy, and therefore have TOA reflectance values above the 15^{th} percentile value, hence they do not cause changes in the binary image. This indicates that the survey shoreline might be constructed based on an average water level that does not match the actual water level of the composite satellite image, which introduces an additional offset. Figure 16 shows the difference between the water level observed at the time instances of the underlying cloud free images within a time window and the water level observed on all underlying images (on which the composite survey shoreline is based in this study). These results indicate that in case a large water level difference is present, the offset is larger compared to small water level differences for a specific image composite. The difference between both water levels decreases with an increasing time window. A longer time window results in more cloud free underlying satellite images. Since a semi-diurnal tidal signal with a spring-neap tidal cycle is present along the Holland coast, more tidal constituents become included in the SDS when more cloud free images are included. The difference between the average water level of all underlying cloud free images and all underlying images therefore reduces, and the additional offset introduced by selecting a different water level for constructing the survey shoreline becomes less pronounced. To correctly average out tidal variations in the SDS position, and to end up with a representation of the SDS at the MSL contour, the time averaging window should be related to the cloud cover near the shoreline, the number of tidal constituents, the timescale of morphological changes and the intertidal beach slope. The intertidal beach slope measured near the first transect is rather mild with an inclination of 1:106 m. The effect of tidal averaging is less pronounced for transects with steeper slopes, for instance along transect 73 with an inter tidal beach slope 1:24 m.

As accuracy seems to be especially limited by the image pixel resolution, a tendency towards higher spatial resolutions, such as the recently launched Sentinel 2 mission or new commercial missions such as the Triplesat with a spatial resolution of 3.2 m indicates a wider application range of satellite imagery in the near future. Besides, better sensor specifications are introduced with the launch of new missions, such as the recently launched geostationary GOES-16 mission with a temporal resolution of 15 minutes or the Landsat 8 mission

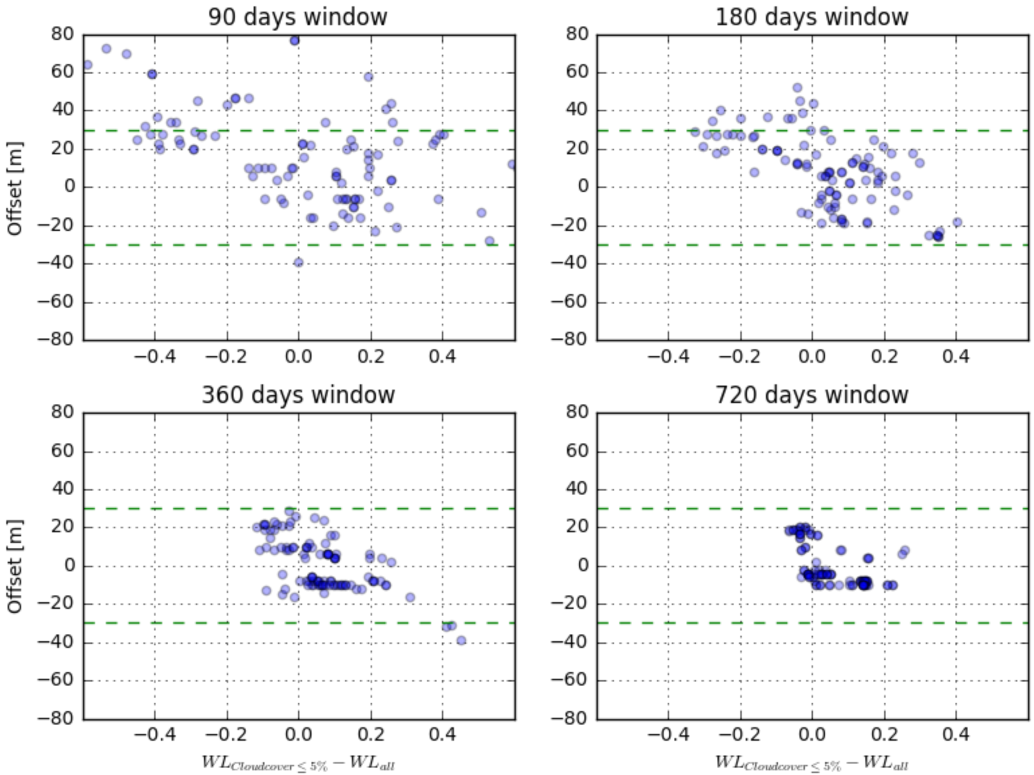

Figure 16: Effect of the image composite moving average time windows on the difference between the water level observed on the underlying cloud free images ($WL_{Cloudcover \leq 5\%}$) and on all underlying images (WL_{all}) within a time window in relation to the offset value. All values are based on the values found at the first transect. The Landsat pixel resolution is indicated in green.

with additional multispectral information. The applicability of the accuracy estimation method described in this study will change with these increasing satellite performances. The reconstruction of the survey shoreline based on a bi-monthly topographic survey that is acquired within 3 days might hamper the offset calculation since for instance local water level deviations or individual wave run-up and run-down becomes more pronounced in the SDS for higher pixel resolutions. This requires even more accurate information on the instantaneous shoreline present during image acquisition. Other methods such as for instance high frequency Argus imagery (Holman & Stanley, 2007) might replace the current method to validate the positional accuracy in case the positional accuracy of new satellite sensors is validated.

Multiple missions of, amongst others, NASA and ESA are currently operational, including missions with active sensors radar sensors such as the Terrasar-X satellite (Vandebroek et al., 2017). Since combing these missions results in more cloud free images near the shoreline, this allows for the opportunity to study coastal evolutions on intra-annual time scales. This also relates to a decreasing moving average time window to obtain cloud free image composites.

6. Conclusions

This paper presents an automated method to extract shorelines from satellite imagery. The accuracy of this method is assessed for the Sand Motor mega-scale nourishment by comparing the Satellite Derived Shorelines (SDS) to topographic surveys. The obtained SDS performs well compared to in-situ measurements of the shoreline. The average accuracy of the SDS for the ideal case of cloud and wave free images for the Sand Motor is 1 m, which is well within the pixel resolution. The accuracy depends on intertidal beach slope and the image pixel resolution.

We have shown that the accuracy decreases in the presence of clouds, waves, sensor corrections and georeferencing errors. This study shows that the most important driver of inaccuracy is cloud cover, which hampers the detection of a SDS and cause large seaward deviations in the order of 200 m, followed by the presence of waves, which cause deviations of about 40 m. A seaward bias of the SDS is always present because all drivers of inaccuracy introduce a seaward shift. Surprisingly the pansharping method, which is intended to increase the image pixel resolution, and hence is expected to increase the accuracy, reduces the accuracy with about a pixel at a sandy shoreline. This indicates that the pansharping technique is not considered suitable for coastal areas.

The found drivers of inaccuracy hamper the application of the SDS in coastal engineering practice because they introduce offsets which makes it impossible to accurately derive trends. Nevertheless, inaccuracies can be overcome by using a moving average image composite window. Although this technique implies a reduction in temporal resolution, it increases the spatial accuracy to subpixel precision (e.g. smaller than 10 - 30 m, depending on the satellite mission), which becomes similar to the benchmark accuracy. This implies that the image composite technique is capable of detecting coastline changes which are at least larger than the pixel resolution.

Given the accuracy of composite images along the Sand Motor in combination with the worldwide availability of public satellite imagery over the past decades and the computational facilities of the Google Earth Engine platform, potentially allows for the application to other coastal areas in the world with large, structural coastline trends as long as the changes are at least in the order of a pixel. Technological progress indicates that the spatial, temporal and spectral resolution of satellite imagery will further increase in the coming years, allowing for potentially even higher accuracies on smaller timescales in the future.

Acknowledgments

This work is funded by the Deltares strategic research program Coastal and Offshore Engineering. Arjen Luijendijk is partially supported by NatureCoast, a project of technology foundation STW, applied science division of the Netherlands Organisation for Scientific Research (NWO). Wiebe de Boer is partially supported by the project Integrated and Sustainable Port development in Ghana within an African context (W07.69.206) within the Urbanizing Deltas of the World programme of NWO. This financial support is highly appreciated by the authors. Furthermore, the authors would like to thank NatureCoast, Rijkswaterstaat and Shore for providing the necessary survey data of the Sand Motor, without which quantifying the SDS accuracy would not have been possible, and Google for providing their cloud computing facilities. Finally, we would also like to thank the two anonymous reviewers for providing their valuable comments, which has significantly improved this manuscript.

References

Almonacid-Caballer, J., Sánchez-García, E., Pardo-Pascual, J. E., Balaguer-Beser, A. A., & Palomar-Vázquez, J. (2016). Evaluation of annual mean shoreline position deduced from Landsat imagery as a mid-term coastal evolution indicator. *Marine Geology*, *372*, 79–88. URL: `http://linkinghub.elsevier.com/retrieve/pii/S0025322715300864`. doi:`10.1016/j.margeo.2015.12.015`.

Bayram, B., Acar, U., Seker, D., & Ari, A. (2008). A Novel Algorithm for Coastline Fitting through a Case Study over the Bosphorus. *Journal of Coastal Research*, *244*, 983–991. URL: `http://www.jcronline.org/doi/abs/10.2112/07-0825.1?code=cerf-site`. doi:`10.2112/07-0825.1`.

Boak, E. H., & Turner, I. L. (2005). Shoreline Definition and Detection: A Review, . *21*, 688–703. URL: `http://www.jcronline.org/doi/full/10.2112/03-0071.1`. doi:`10.2112/03-0071.1`.

Booij, N., Ris, R., & Holthuijsen, L. H. (1999). A third-generation wave model for coastal regions. I- Model description and validation. *Journal of geophysical research*, *104*, 7649–7666. URL: `http://onlinelibrary.wiley.com/doi/10.1029/98JC02622/full`. doi:`10.1029/98jc02622`.

Donchyts, G., Baart, F., Winsemius, H., Gorelick, N., Kwadijk, J., & van de Giesen, N. (2016). Earth's surface water change over the past 30 years. *Nature Clim. Change*, *6*, 810–813. URL: `http://www.nature.com/nclimate/journal/v6/n9/full/nclimate3111.html`. doi:`10.1038/nclimate3111`.

García-Rubio, G., Huntley, D., & Russell, P. (2015). Evaluating shoreline identification using optical satellite images, . *359*, 96–105. URL: `http://www.sciencedirect.com/science/article/pii/S0025322714003259`. doi:`10.1016/j.margeo.2014.11.002`.

Goodchild, M. F., & Hunter, G. J. (1996). A simple positional accuracy measure for linear features. *International Journal Geographical information science*, *11*, 299–306. URL: http://dx.doi.org/10.1080/136588197242419. doi:10.1080/136588197242419.

Gorelick, N., Hancher, M., Dixon, M., Ilyushchenko, S., Thau, D., & Moore, R. (2017). Google earth engine: Planetary-scale geospatial analysis for everyone. *Remote Sensing of Environment*, . URL: https://doi.org/10.1016/j.rse.2017.06.031. doi:10.1016/j.rse.2017.06.031.

Hansen, M. C., Potapov, P. V., Moore, R., Hancher, M., Turubanova, S. A., Tyukavina, A., Thau, D., Stehman, S. V., Goetz, S. J., Loveland, T. R., Kommareddy, A., Egorov, A., Chini, L., Justice, C. O., & Townshend, J. R. G. (2013). High-Resolution Global Maps of 21st-Century Forest Cover Change. *Science*, *342*, 850–853. URL: http://www.sciencemag.org/cgi/doi/10.1126/science.1244693. doi:10.1126/science.1244693.

Holman, R., & Stanley, J. (2007). The history and technical capabilities of argus. *Coastal Engineering*, *54*, 477–491. URL: http://www.sciencedirect.com/science/article/pii/S037838390700018X. doi:10.1016/j.coastaleng.2007.01.003.

Kamdi, S., & Krishna, R. K. (2011). Image Segmentation and Region Growing Algorithm. *International Journal of Computer Technology and Electronics Engineering*, *2*, 103–107. URL: http://www.ijctee.org/files/VOLUME2ISSUE1/IJCTEE_0212_18.pdf.

Kuleli, T., Guneroglu, A., Karsli, F., & Dihkan, M. (2011). Automatic detection of shoreline change on coastal Ramsar wetlands of Turkey. *Ocean Engineering*, *38*, 1141–1149. URL: http://dx.doi.org/10.1016/j.oceaneng.2011.05.006. doi:10.1016/j.oceaneng.2011.05.006.

Liu, Q., Trinder, J., & Turner, I. L. (2017). Automatic super-resolution shoreline change monitoring using Landsat archival data: a case study at

NarrabeenCollaroy Beach, Australia. *Journal of Applied Remote Sensing*, *11(1)*. doi:10.1117/1.JRS.11.016036.

Mantz, H., Jacobs, K., & Mecke, K. (2008). Utilizing Minkowski functionals for image analysis: a marching square algorithm. *Journal of Statistical Mechanics: Theory and Experiment*, (p. P12015). URL: http://stacks.iop.org/1742-5468/2008/i=12/a=P12015. doi:10.1088/1742-5468/2008/12/P12015.

Mcfeeters, S. K. (1996). The use of the normalized difference water index (ndwi) in the delineation of open water features. *International Journal of Remote Sensing*, *17*, 1425–1432. URL: http://dx.doi.org/10.1080/01431169608948714. doi:10.1080/01431169608948714.

Minneboo, F. (1995). *Jaarlijkse kustmetingen*. Technical Report april. doi:uuid:76f2634d-f3c4-4609-aa4c-44d641da28f1.

Otsu, N. (1979). Smith et al. - 1979 - A Tlreshold Selection Method from Gray-Level Histograms. *IEEE TRANSACTIONS ON SYSTREMS, MAN, AND CYBERNETICS,*, *9*, 62–66. doi:10.1109/TSMC.1979.4310076.

Pardo-Pascual, J. E., Almonacid-Caballer, J., Ruiz, L. A., & Palomar-Vázquez, J. (2012). Automatic extraction of shorelines from Landsat TM and ETM+ multi-temporal images with subpixel precision. *Remote Sensing of Environment*, *123*, 1–11. URL: http://dx.doi.org/10.1016/j.rse.2012.02.024. doi:10.1016/j.rse.2012.02.024.

Pianca, C., Holman, R., & Siegle, E. (2015). Shoreline variability from days to decades: Results of long-term video imaging. *Journal of Geophysical Research C: Oceans*, *120*, 2159–2178. doi:10.1002/2014JC010329.

Radermacher, M., de Schipper, M., Swinkels, C., MacMahan, J., & Reniers, A. (2017). Tidal flow separation at protruding beach nourishments. *Journal of Geophysical Research C: Oceans*, *122*, 63–79. doi:10.1002/2016JC011942.

Ruggiero, P., Kaminsky, G. M., Gelfenbaum, G., & Voigt, B. (2005). Seasonal to Interannual Morphodynamics along a High-Energy Dissipative Littoral Cell. *Journal of Coastal Research*, *213*, 553–578. URL: `http://www.bioone.org/doi/abs/10.2112/03-0029.1`. doi:`10.2112/03-0029.1`.

de Schipper, M. A., de Vries, S., Ruessink, G., de Zeeuw, R. C., Rutten, J., van Gelder-Maas, C., & Stive, M. J. F. (2016). Initial spreading of a mega feeder nourishment: Observations of the Sand Engine pilot project. *Coastal Engineering*, *111*, 23–38. URL: `http://dx.doi.org/10.1016/j.coastaleng.2015.10.011`. doi:`10.1016/j.coastaleng.2015.10.011`.

Stive, M. J., de Schipper, M. a., Luijendijk, A. P., Aarnikhof, S. G., van Gelder-Maas, C., van Thiel de Vries, J. S., de Vries, S., Henriquez, M., Marx, S., & Ranasinghe, R. (2013). A new alternative to saving our beaches from sea-level rise: the sand engine. *Journal of Coastal Research*, *29*, 1001–1008. URL: `http://www.jcronline.org/doi/abs/10.2112/JCOASTRES-D-13-00070.1`. doi:`10.2112/JCOASTRES-D-13-00070.1`.

Thieler, E., Himmelstoss, E., Zichichi, J., & Ergul, A. (2009). *Digital Shoreline Analysis System (DSAS) version 4.0 An ArcGIS extension for calculating shoreline change: U.S. Geological Survey Open-File Report*. Technical Report USGS.

Turner, I. L., Harley, M. D., Short, A. D., Simmons, J. A., Bracs, M. A., Phillips, M. S., & Splinter, K. D. (2016). A multi-decade dataset of monthly beach profile surveys and inshore wave forcing at Narrabeen, Australia., . *3*, 160024. URL: `https://www.nature.com/articles/sdata201624`. doi:`10.1038/sdata.2016.24`.

USGS (2008). *Global Land Survey Digital Elevation Model (GLSDEM)*. Technical Report.

Vandebroek, E., Lindenbergh, R., van Leijen, F., de Schipper, M., de Vries, S., & Hanssen, R. (2017). Semi-automated monitoring of a mega-scale beach nourishment using high-resolution terrasar-x satellite data. *Remote Sensing*, *9*. URL: http://www.mdpi.com/2072-4292/9/7/653. doi:10.3390/rs9070653.

Wijedasa, L. S., Sloan, S., Michelakis, D. G., & Clements, G. R. (2012). Overcoming limitations with landsat imagery for mapping of peat swamp forests in sundaland. *Remote Sensing*, *4*, 2595–2618. URL: http://www.mdpi.com/2072-4292/4/9/2595. doi:10.3390/rs4092595.

Wijnberg, K. M. (2002). Environmental controls on decadalmorphologic behaviour of the Holland coast. *Marine Geology*, *189*, 227–247. URL: http://www.sciencedirect.com/science/article/pii/S0025322702004802. doi:doi:10.1016/S0025-3227(02)00480-2.

Zhu, Z., Wang, S., & Woodcock, C. E. (2015). Improvement and expansion of the Fmask algorithm: Cloud, cloud shadow, and snow detection for Landsats 4-7, 8, and Sentinel 2 images. *Remote Sensing of Environment*, *159*, 269–277. URL: http://www.sciencedirect.com/science/article/pii/S0034425714005069. doi:10.1016/j.rse.2014.12.014.